FESSTVaL

The Field Experiment on Submesoscale Spatio-Temporal Variability in Lindenberg

Cathy Hohenegger, Felix Ament, Frank Beyrich, Ulrich Löhnert, Henning Rust, Jens Bange, Tobias Böck, Christopher Böttcher, Jakob Boventer, Finn Burgemeister, Marco Clemens, Carola Detring, Igor Detring, Noviana Dewani, Ivan Bastak Duran, Stephanie Fiedler, Martin Göber, Chiel van Heerwaarden, Bert Heusinkveld, Bastian Kirsch, Daniel Klocke, Christine Knist, Ingo Lange, Felix Lauermann, Volker Lehmann, Jonas Lehmke, Ronny Leinweber, Kristina Lundgren, Matthieu Masbou, Matthias Mauder, Wouter Mol, Hannes Nevermann, Tatiana Nomokonova, Eileen Päschke, Andreas Platis, Jens Reichardt, Luc Rochette, Mirjana Sakradzija, Linda Schlemmer, Jürg Schmidli, Nima Shokri, Vincent Sobottke, Johannes Speidel, Julian Steinheuer, David D. Turner, Hannes Vogelmann, Christian Wedemeyer, Eduardo Weide-Luiz, Sarah Wiesner, Norman Wildmann, Kevin Wolz, and Tamino Wetz

KEYWORDS: Atmosphere; Cold pools; Remote sensing; Surface observations; Model evaluation/ performance; Field experiments

ABSTRACT: Numerical weather prediction models operate on grid spacings of a few kilometers, where deep convection begins to become resolvable. Around this scale, the emergence of coherent structures in the planetary boundary layer, often hypothesized to be caused by cold pools, forces the transition from shallow to deep convection. Yet, the kilometer-scale range is typically not resolved by standard surface operational measurement networks. The measurement campaign Field Experiment on Submesoscale Spatio-Temporal Variability in Lindenberg (FESSTVaL) aimed at addressing this gap by observing atmospheric variability at the hectometer-to-kilometer scale, with a particular emphasis on cold pools, wind gusts, and coherent patterns in the planetary boundary layer during summer. A unique feature was the distribution of 150 self-developed and low-cost instruments. More specifically, FESSTVaL included dense networks of 80 autonomous cold pool loggers, 19 weather stations, and 83 soil sensor systems, all installed in a rural region of 15-km radius in eastern Germany, as well as self-developed weather stations handed out to citizens. Boundary layer and upper-air observations were provided by eight Doppler lidars and four microwave radiometers distributed at three supersites; water vapor and temperature were also measured by advanced lidar systems and an infrared spectrometer; and rain was observed by a X-band radar. An uncrewed aircraft, multicopters, and a small radiometer network carried out additional measurements during a 4-week period. In this paper, we present FESSTVaL's measurement strategy and show first observational results including unprecedented highly resolved spatiotemporal cold-pool structures, both in the horizontal as well as in the vertical dimension, associated with overpassing convective systems.

AFFILIATIONS: Hohenegger—Max Planck Institute for Meteorology, and Hans Ertel Centre for Weather Research, Hamburg, Germany; **Ament, Kirsch, Lundgren, and Wiesner**—Meteorological Institute, University of Hamburg, and Hans Ertel Centre for Weather Research, Hamburg, Germany; **Beyrich, C. Detring, Knist, Lauermann, Lehmann, Leinweber, Päschke, and Reichardt**—Meteorological Observatory Lindenberg-Richard Aßmann Observatory, Deutscher Wetterdienst, Lindenberg, Germany; **Löhnert, Fiedler, Steinheuer, and Weide-Luiz**—Institute for Geophysics and Meteorology, University of Cologne, and Hans Ertel Centre for Weather Research, Cologne, Germany; **Rust, Böttcher, Lehmke, and Sobottke**—Institute for Meteorology, Freie Universität Berlin, and Hans Ertel Centre for Weather Research, Berlin, Germany; **Bange, Boventer, and Platis**—Environmental Physics, GUZ, University of Tübingen, Tübingen, Germany; **Böck, Nomokonova, and Wedemeyer**—Institute for Geophysics and Meteorology, University of Cologne, Cologne, Germany; **Burgemeister, Clemens, and Lange**—Meteorological Institute, University of Hamburg, Hamburg, Germany; **I. Detring and Schlemmer**—Deutscher Wetterdienst, Offenbach, Germany; **Dewani, Duran, and Schmidli**—Faculty of Geosciences and Geography, Institute for Atmospheric and Environmental Sciences, Goethe University Frankfurt, and Hans Ertel Centre for Weather Research, Frankfurt, Germany; **Göber, Klocke, and Sakradzija**—Hans Ertel Centre for Weather Research, Offenbach, Germany; **van Heerwaarden, Heusinkveld, and Mol**—Meteorology and Air Quality Group, Wageningen University, Wageningen, Netherlands; **Masbou**—Deutscher Wetterdienst, and Hans Ertel Centre for Weather Research, Offenbach, Germany; **Mauder**—TU Dresden, Dresden, Germany; **Nevermann and Shokri**—Institute of Geo-Hydroinformatics, Hamburg University of Technology, Hamburg, Germany; **Rochette**—LR Tech Inc., Lévis, Quebec, Canada; **Speidel, Vogelmann, and Wolz**—Institute of Meteorology and Climate Research–Atmospheric Environmental Research (IMK-IFU), Karlsruhe Institute of Technology, Garmisch-Partenkirchen, Germany; **Turner**—NOAA/Global Systems Laboratory, Boulder, Colorado; **Wildmann and Wetz**—Institute of Atmospheric Physics, Deutsches Zentrum für Luft- und Raumfahrt e.V., Oberpfaffenhofen, Germany
Duran's current affiliation: European Centre for Medium-Range Weather Forecasts, Bonn, Germany.
Fiedler's current affiliation: GEOMAR Helmholtz Centre for Ocean Research Kiel and Christian-Albrechts-University of Kiel, Kiel, Germany.
Klocke's current affiliation: Max Planck Institute for Meteorology, Hamburg, Germany. Nomokonova's current affiliation: RPG Radiometer Physics GmbH, Meckenheim, Germany. Steinheuer's current affiliation: Institute of Geosciences, Department of Meteorology, University of Bonn, Bonn, Germany.

Mature organized thunderstorms are impressive weather systems extending over hundreds to thousands of kilometers. Despite their spatial coherence, such systems are not internally homogeneous, but made of individual building blocks, the convective cell, with an equivalent diameter of only a few kilometers (Houze 2004). Moreover, before reaching such impressive sizes, thunderstorms have to grow out of small shallow convective clouds. This transition happens at the kilometer scale in idealized simulations (e.g., Grabowski et al. 2006; Böing et al. 2012; Morrison et al. 2022) and is thought to involve the generation of cold pools (Khairoutdinov and Randall 2006; Schlemmer and Hohenegger 2014; Hirt et al. 2020). Cold pools result from the evaporation and melting of hydrometeors in and below convective clouds. The associated latent cooling leads to the formation of negatively buoyant air that sinks through the atmospheric column and propagates at the surface like a density current, a current loosely referred to as a cold pool given its relatively low temperature compared to the warm environment (Drager and van den Heever 2017;

Rochetin et al. 2021). Cold pools are efficient at triggering deeper and bigger convective cells at their edges (Khairoutdinov and Randall 2006; Schlemmer and Hohenegger 2014). At the time of the transition from shallow to deep convection, cold pools are also small, with a radius below 1 km (Fig. 6 in Schlemmer and Hohenegger 2014).

Reflecting these considerations, from a weather forecasting or climate modeling perspective, it is generally thought that the discretized fluid-dynamical equations can begin to represent convective motions when using kilometer-scale grid spacings. The first limited-area weather forecasts and regional climate model simulations conducted at such grid spacings appeared about 20 years ago (Mass et al. 2002; Grell et al. 2000). Nowadays, more and more climate modeling centers are even able to conduct kilometer-scale simulations over the full Earth (Stevens et al. 2019).

Despite the obvious importance of the kilometer scale, observations at kilometer scale are lacking. In Germany, the mean distance between the stations of the operational surface net-work is approximately 25 km. Likewise, the well-known Oklahoma Mesonet (Brock et al. 1995; Mc Pherson et al. 2007), often employed to study thunderstorms, captures the surface meteorology every ~35 km. To enhance the spatial resolution, past field campaigns have used radars, Doppler lidars, and uncrewed aircrafts (e.g., Wakimoto 1982; Soderholm et al. 2016; Houston et al. 2012), approaches which nevertheless do not provide information close to the surface. Higher-resolution surface-based observations can be obtained from the mobile mesonet (Straka et al. 1996), with a fleet limited to 15 automobiles, or personal weather stations (Clark et al. 2018; Mandement and Caumont 2020), with the downside of a low sampling frequency (at best 5 min) and a poor coverage in rural areas. To resolve small-scale heterogeneity in updrafts and cold pools, the recent C^3LOUD-Ex campaign experimented with a flying curtain of two to three stationary drones deployed over a horizontal distance of 100 m to 1 km (see Fig. 5 in van den Heever et al. 2021). Observing the atmosphere at kilometer scales from the surface remains challenging.

The Field Experiment on Submesoscale Spatio-Temporal Variability in Lindenberg (FESSTVaL) took place from 17 May to 27 August 2021 in the area around the Meteorological Observatory Lindenberg–Richard Aßmann Observatory (MOL-RAO) of the German Meteorological Service (Deutscher Wetterdienst, DWD), about 60 km southeast of Berlin (Germany). The overall goal of FESSTVaL was to observe submesoscale atmospheric variability. Submesoscale variability is here loosely defined as variability occurring on scales smaller than 10 km.

FESSTVaL had three more specific goals:

1) Measure submesoscale variability: to overcome the observational challenges of measuring submesoscale variability, FESSTVaL employed a combination of low-cost, self-developed instruments and well-established, commercial instruments, including citizen participation, to sample the atmosphere at high spatial and temporal resolution. FESSTVaL also developed and tested new retrieval algorithms from ground-based remote sensing instruments to gain insight into the vertical variability of atmospheric variables generally not retrieved by commercially available algorithms.
2) Quantify submesoscale variability: several atmospheric processes can generate submesoscale variability in the planetary boundary layer during summertime. FESSTVaL focused on characterizing the three-dimensional spatial structure of cold pools; the spatial variability of wind gusts, which often accompany cold pools; and the spatial scales of coherent structures in the clear and nonprecipitating cloud-topped planetary boundary layer, which may precede the development of thunderstorms and cold pools. Further interests included quantification of submesoscale variability in radiation, in the nighttime low-level jet and in soil moisture, the latter in view of developing predictive tools to quantify soil moisture dynamics using machine learning algorithms.

3) Validate the representation of submesoscale variability in atmospheric models: focus was on atmospheric models run with a grid spacing of $O(100)$ m to $O(10)$ km.

Measuring submesoscale variability

The area around MOL-RAO is rural with forests, agricultural fields, and lakes dominating the landscape (see Fig. 2 in Beyrich et al. 2002). Surface elevation varies between 40 and 130 m in a gently undulating topography. This lack of strong orographical influence, combined with a relatively high likelihood for thunderstorm development and the presence of DWD's supersite, motivated the choice of MOL-RAO as center of operation. FESSTVaL's measure-ment strategy (see Fig. 1) combined a dense network of surface observations with a verti-cal sampling of the atmosphere. The surface observations were deployed within a circle of 15-km radius around the boundary layer field site (in German: Grenzschichtmessfeld, GM) Falkenberg of DWD. They formed what we call the FESSTVaL circle. The vertical sampling was performed at the three supersites GM Falkenberg, Lindenberg, and Birkholz, forming what we call the FESSTVaL triangle. The achieved spatial resolution in the FESSTVaL circle ranged between 100 m and 5 km, whereas the edge length of the triangle was 5–6 km.

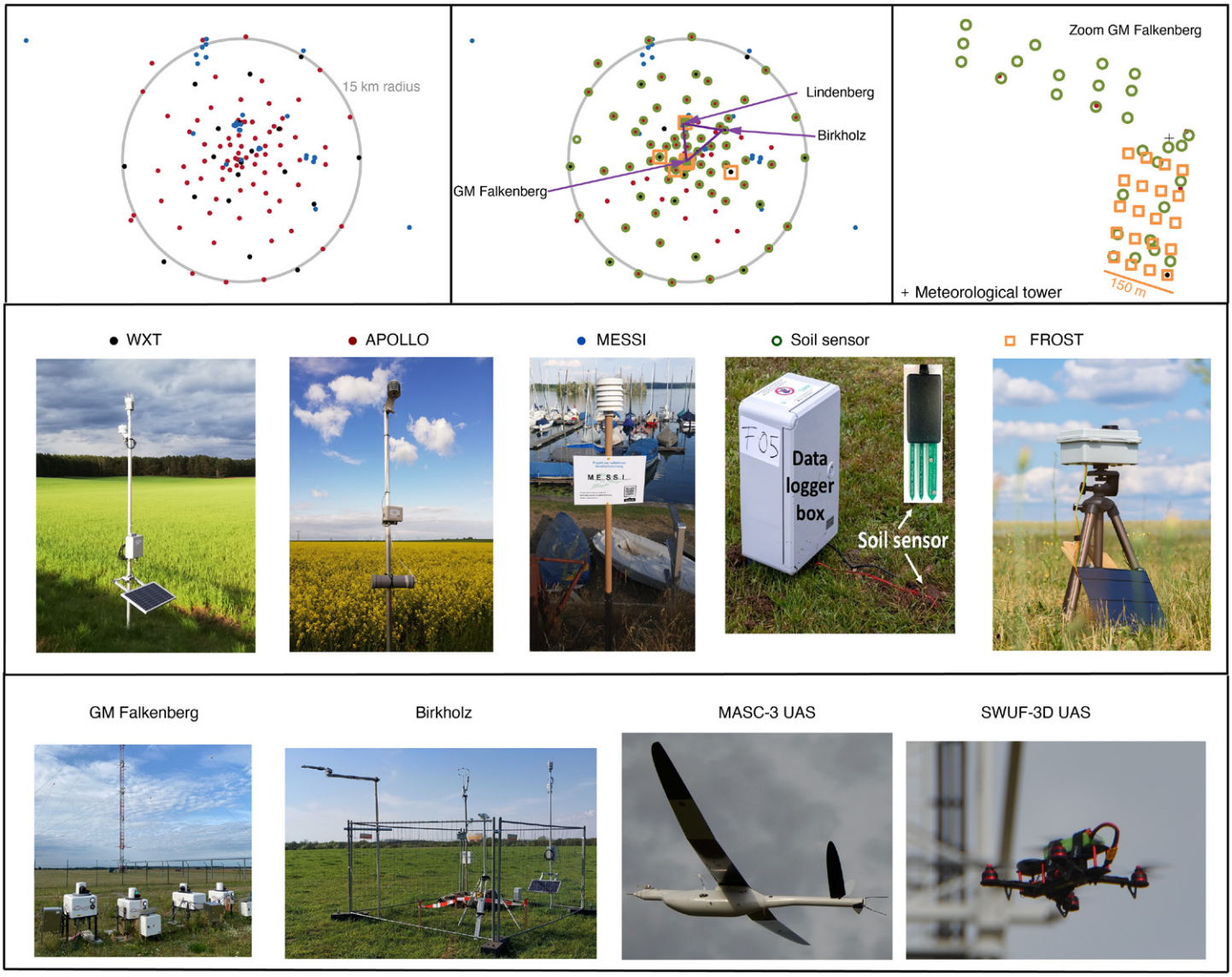

Fig. 1. Deployment of instruments. (top left) Given the number of instruments and for clarity, we only shows the locations of APOLLOs, WXTs, and MESSIs. (top center) The locations of soil sensors, FROSTs, and of the three supersites. (top right) A zoom on the GM Falkenberg site to reveal the denser network at that site.

Additional instruments were located at GM Falkenberg to get more information on vari-ability on scales smaller than 100 m. On top of that, FESSTVaL could rely on the routine measurement program of MOL-RAO (see https://www.dwd.de/EN/research/observing_atmosphere/lindenberg_column/lindenberg_column_node.html). The MOL-RAO instrumentation includes a 99-m tower at GM Falkenberg and a suite of ground-based remote sensing systems at Lindenberg.

The FESSTVaL circle. WXTs, APOLLOs, MESSIs, FROSTs, and soil sensors monitored the near-surface state of the atmosphere and of the soil during FESSTVaL (see Fig. 1 and Table A1 in appendix A for a detailed description of the instruments). The WXT weather sta-tions record basic meteorology in terms of temperature, pressure, relative humidity, wind speed, wind direction, and precipitation. Solar panels ensured their power supply. WXTs are widely used commercial instruments, but their cost limits the number of stations within a network. Nineteen instruments were deployed during FESSTVaL (Kirsch et al. 2022a), with distances ranging between 1.5 and 9.6 km, giving a median distance of 4.9 km.

To augment this spatial resolution, 80 Autonomous Cold Pool Loggers (APOLLOs) were added to the network (Kirsch et al. 2022a). The spatial density diminished from the center of the FESSTVaL circle (100 m) toward its edge (4.8 km). The median distance was 1.8 km. APOLLOs are self-developed instruments, with a cost of around 300 euros per station; see Kirsch et al. (2022b) for a comprehensive description of the instruments. APOLLOs measure temperature and pressure, two quantities that are straightforward to measure at low cost and allow a reliable detection of cold pools, as demonstrated by Kirsch et al. (2022b) in a preparatory field campaign to FESSTVaL. A battery provides the necessary power, but the battery needs to be changed every 10–14 days. This makes APOLLOs maintenance intensive. Servicing all stations resulted in a tour of about 350 km. This effort limited the area that could be covered by APOLLOs.

To partly remedy this drawback, the spatial coverage of the network was extended by add-ing MESSIs. These are low-cost weather stations designed and premanufactured in-house, see Kox et al. (2021). MESSIs measure temperature, relative humidity, pressure, and radia-tion. They were distributed to citizens who live in the region. Citizens were recruited through advertisement of the project in a local newspaper, in a local radio channel, on a poster at the local weather museum, and by word-of-mouth by the staff of MOL-RAO. At the end, there were more requests for participation than devices available. Involving citizens (see appendix B about citizen science in general) implies the risk of suboptimal assembly, placement, and maintenance, although the citizens were guided on those aspects during a virtual workshop, and provided with a manual and an email hotline. The Long Range Wide Area Network tech-nology transferred the data in near–real time. Data can be visualized with a web application. MESSIs, APOLLOs, and WXTs were collocated at a few locations to check accuracy given the instruments' strengths and weaknesses. Observations from WXTs, APOLLOs, and MESSIs were employed to characterize the submesoscale variability associated with cold pools, whereas WXTs also provided information on wind gust variability.

Most WXTs and APOLLOs were paired with commercial soil sensors to study interactions between cold pools and the surface. The soil sensors were placed at the surface to measure skin temperature and at 11 cm below the surface to measure temperature and soil moisture. A battery, which has a lifetime of about 1 month at a measurement sampling rate of 5 min, provided the power supply. Additionally, 29 soil sensors were deployed at GM Falkenberg, with distances of $O(50)$ m. The aim was to capture variability at scales smaller than in the FESSTVaL circle as soil moisture is known to be highly variable. Finally, an energy balance station was located in Birkholz to provide further information on land–atmosphere interac-tions via measurements of surface fluxes (Lange and Ament 2022).

From 14 to 29 June, 20 instruments called FROSTs, the Fast Response Optical Spectros-copy Time synchronized instruments, were added to the GM Falkenberg field, arranged in a 200 m × 150 m rectangle with 50-m spacing between the instruments. Four additional instruments were placed at a distance of 5 km around GM Falkenberg. FROST measures solar irradiance at very high frequency; see Heusinkveld et al. (2022). A small solar panel ensures the power supply. Again, the design of FROST resulted from the needs to develop low-cost instruments to capture submesoscale variability. During FESSTVaL, the focus was on capturing variability in irradiance and in integrated water vapor for clear-sky days (Mol and Heusinkveld 2022).

The FESSTVaL triangle. The vertical profiling of the atmosphere was performed at the corners of the FESSTVaL triangle (see Table A2). Four microwave radiometers (Löhnert et al. 2022) and eight Doppler wind lidars (Detring et al. 2023; Päschke 2022; Dewani and Leinweber 2022; Leinweber et al. 2023) continuously sampled the vertical profiles of temperature, humidity, and wind. Microwave radiometers can sample the whole atmospheric column, even though the information content rapidly decreases with height, whereas the range of Doppler wind lidars is mostly confined to the boundary layer as they rely on particle backscattering. We ensured that temperature and wind gusts were retrieved at each corner of the FESSTVaL triangle given the scientific interests of FESSTVaL. Temperature profiles were derived from elevation scans of the microwave radiometers according to Crewell and Löhnert (2007). Concerning wind gust retrievals, Suomi et al. (2017) were the first to show that wind gusts can be derived from Doppler wind lidars with high accuracy. However, due to the use of a different type of Doppler wind lidar, we had to design a new scan configuration and new retrieval algorithms (see Steinheuer et al. 2022; Detring et al. 2022). The new beam swinging configuration con-sists of a conical fast continuous scanning mode with one scan circle completed within 3.4 s.

Three additional Doppler wind lidars were operated at GM Falkenberg in special con-figurations to provide a more complete picture of the boundary layer dynamics, namely, by measuring vertical wind velocity (Dewani and Leinweber 2022), turbulent kinetic energy, and momentum fluxes (Päschke 2022) as well as by horizontally scanning the wind field. Turbulent kinetic energy was derived from a slow continuous scanning mode using the al-gorithm suggested by Smalikho and Banakh (2017). Mean wind is available from the lidars scanning in fast and slow modes (Detring et al. 2023; Päschke 2022) as well as from two extra Doppler lidars located in Lindenberg and GM Falkenberg (Leinweber et al. 2023). As a measure of quality assurance, the Doppler wind lidars were moved to GM Falkenberg from 15 July to 9 August and operated side by side to compare their performance characteristics. Also, due to instrument failures and other campaign requirements, not all the Doppler wind lidars were available during the whole campaign.

An Atmospheric Sounder Spectrometer by Infrared Spectral Technology (ASSIST; Turner and Rochette 2022) as well as the ATMONSYS lidar system augmented the microwave radiometer observations at Lindenberg. ASSIST measures downwelling infrared spectra, from which thermodynamic profiles were retrieved using Tropospheric Remotely Observed Profiling via Optimal Estimation (TROPoe), as described in Turner and Löhnert (2021). ATMONSYS measures temperature, water vapor, and aerosol profiles. ASSIST has a higher information content than the microwave radiometers for both temperature and humidity, and FESSTVaL provided the opportunity to more thoroughly evaluate the potential for syn-ergy between instruments. Finally, we complemented the operational radiosondes of DWD with additional launches on days with flight operations or with forecasted thunderstorm activity [see Table A3 and Kirsch et al. (2022c)].

Uncrewed aerial systems further augmented the sampling of the small-scale variability in the planetary boundary layer, both horizontally and vertically, with measurements of

pressure, temperature, humidity, and wind. First, the SWUF-3D fleet of quattrocopters (Wildmann 2022) was operated at GM Falkenberg from 21 June to 2 July in one of five pre-defined flight patterns according to an intended mission type [see Table A4 and Fig. 1 in Wetz et al. (2023)]. The decision was made on a day-to-day basis taking into account the fore-casted weather conditions. One hundred twenty-four formation flights were conducted with a maximum of 21 drones flying simultaneously. The horizontal range of the measurements was a few hundreds of meters. Wetz et al. (2021) and Wildmann and Wetz (2022) showed that the fleet can well reproduce meteorological tower measurements, whereas Wetz et al. (2023) showed first results on coherence in planetary boundary layer flows on the microscale. A second larger uncrewed aircraft called MASC-3 performed 47 flights between 7 June and 2 July (Jung et al. 2023). MASC-3 is described in Rautenberg et al. (2019). It flew in one of two flight patterns with flight duration of about 75 min each (see Table A5). MASC-3 covered a horizontal distance of 2.5–3 km and sampled the full planetary boundary layer up to 2.5 km above the ground. The measurements were validated against the DWD operational tower measurements at 90.3 m above ground level. Otherwise, MASC-3 was employed to validate some of the novel lidar retrieval algorithms, to characterize the vertical mean and turbulent structure of the convective planetary boundary layer and to capture coherent patterns.

Finally, an X-band radar was deployed at GM Falkenberg to monitor rainfall rates at high spatiotemporal resolution (Burgemeister et al. 2022), with a 20-km scan radius. The X-band radar operates following Lengfeld et al. (2014), and observations were calibrated and validated with operational micro rain radar measurements located in Lindenberg.

Quantifying submesoscale variability

An overview of the occurrence of the processes targeted during FESSTVaL together with their definition is given in Fig. 2. FESSTVaL experienced 32 days with cold pools, 20 days with wind gusts, and 55 days with low-level jets. To give some context, looking back at the preparatory field campaigns from 2020, Kirsch et al. (2022b) reported 28 days with cold pools in Hamburg for 3 months, whereas Weide Luiz and Fiedler (2022) diagnosed 13% less low-level jets in Lindenberg. On 7 days, the planetary boundary layer had almost no cloud, whereas on 31 days it was topped with nonprecipitating clouds. Having observed more than a few events gives us some insight into the internal variability of the targeted processes. For instance, the strength of cold pools, as quantified by the maximum recorded temperature perturbation per event, varied between 2.8 and 11.1 K with a median of 5.1 K. As a comparison, Kirsch et al. (2021) and Kruse et al. (2022) using long-term tower observations during summertime in Hamburg and Cabauw, respectively, found a median temperature perturbation of 3.3 and 2.9 K. The maximum recorded wind gust at a height of 90.3 m was 19.1 m s^{-1}, and half of the wind gusts were recorded on cold pool days, even though only 10 of the 32 cold pool days had wind gusts fulfilling our wind gust criterium. Wind gusts recorded on cold pool days were slightly stronger than wind gusts recorded on other days, with a mean of 16.5 m s^{-1} versus 15.6 m s^{-1}, and they lasted in mean about half as long.

The long measurement period allowed to capture temporal variability, but the main goal of FESSTVaL was to capture submesoscale variability in space. To show first results, we peer into the three-dimensional structure of one example cold pool that occurred on 29 June 2021. We choose that event as it was a strong and impressive event, with the strongest recorded temperature perturbation, and it also occurred at the time when all instruments were in operation.

After the development of a well-mixed boundary layer in the morning with relatively small temperature variability across the FESSTVaL circle (Fig. 3), convective activity in the region led to the development of a pronounced cold pool. Its signature is visible by the strong and sudden temperature drop around 1330 UTC. The strongest recorded cooling is around 11 K,

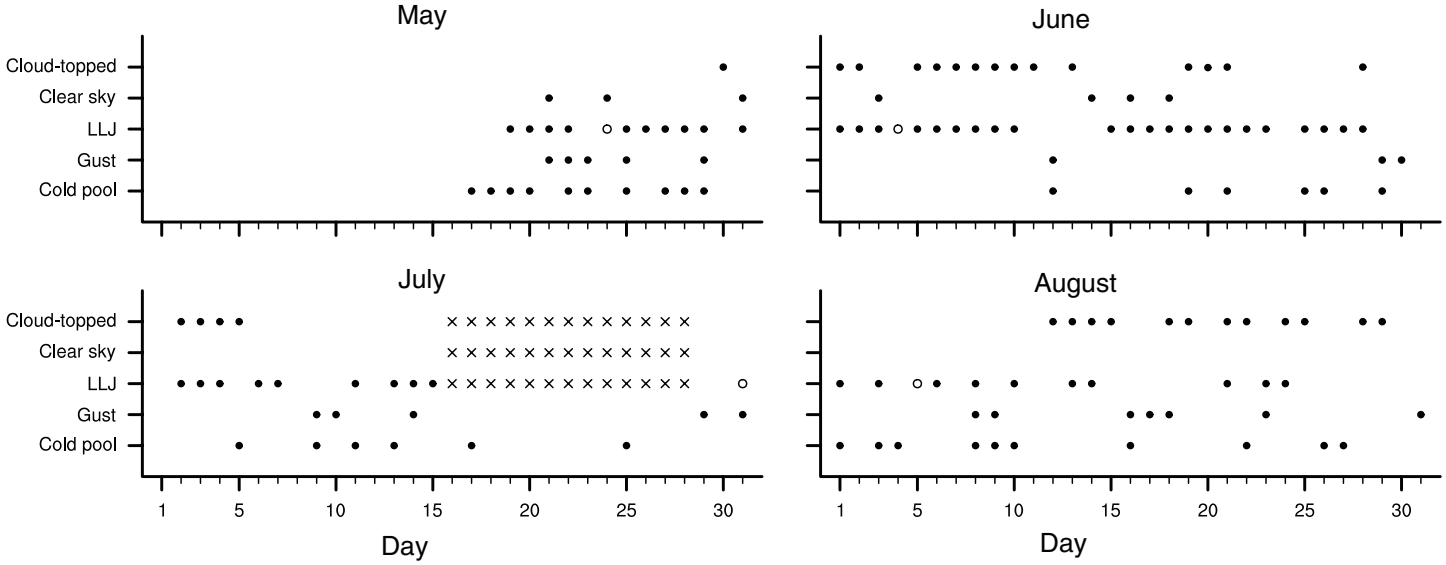

Fig. 2. Event overview with events identified as follows. Cold pool: presence of a temperature drop of at least 2 K within 20 min recorded at at least five APOLLO/WXT stations within 1 h (following Kirsch et al. 2022b) and checked against radar and campaign log book for plausibility. A cold pool event is assumed to last for at least 4 h, it can contain single or multiple cold pools, and the cold pool does not have to be fully within the FESSTVaL circle. Gust: daily maximum wind of 3-s moving average from sonic measurements at GM Falkenberg at 90.3 m larger than 14 m s^{-1}, whereby this threshold is employed by DWD to issue its first-level gust warning. Low-level jet (LLJ): detected according to Weide Luiz and Fiedler (2022) with filled symbols for initial detection time in the evening (before 0000 UTC), open symbols in the morning (after 0000 UTC), and a cross for no data during part of the lidar intercomparison exercise. Clear sky: predominantly clear during daytime using Doppler lidar in vertical stare mode at GM Falkenberg. Cloud-topped: presence of clouds during the day without rain.

but a large variability exists across the network. The large variability relates to the fact that the core of the cold pool, with a temperature perturbation larger than 10 K, never extended for more than 10 km in one direction during its life cycle. Also, the convective activity remained restricted to the eastern, and later on northeastern, side of the FESSTVaL circle. As a conse-quence, stations with summertime temperatures of more than 30°C coexisted with stations displaying temperatures below 20°C. Figure 4b reveals a very sharp temperature gradient between the cold pool and its warm environment, with a 9 K decrease over 7 km.

On the one hand, this sharp gradient and the small size of the cold pool core speak for using a high-density observational network. On the other hand, the internal horizontal structure of the cold pool appears rather homogeneous in Fig. 4. It is made of a cold core and almost equally spaced isotherms of decreasing temperature perturbation toward the warm environ-ment. The cold core matches perfectly with the area of the strongest precipitation, especially at the beginning of the convective life cycle (Fig. 4a) as merging of cells complicates the picture later on (Fig. 4b). But not surprisingly (e.g., Wakimoto 1982), the cold pool extends over an area larger than the precipitating area. The propagation velocity of the cold pool can be easily determined from the time lag in temperature drop across stations due to the high density of our measurements. For the two example stations shown in Fig. 3, a propagation velocity of 6.2 m s^{-1} is derived. As a last geometrical characteristic, the captured cold pool is not round, as assumed in some recently proposed conceptual models of cold pools based on idealized simulations (Haerter et al. 2019; Romps and Jeevanjee 2019). Instead, cold pools tend to elongate in the direction of the mean wind as found in previous observations of mesoscale convective systems (Corfidi 2003).

The FESSTVaL triangle captured the imprint of the cold pool in the vertical (see Fig. 5, bottom row). The sharp temporal drop in temperature associated with the cold pool is clear-est in the lowest 500 m, with only weaker signatures up to 1 km, giving a cold pool depth of 500 m to 1 km. Similar to what was found in previous studies based on tower observations

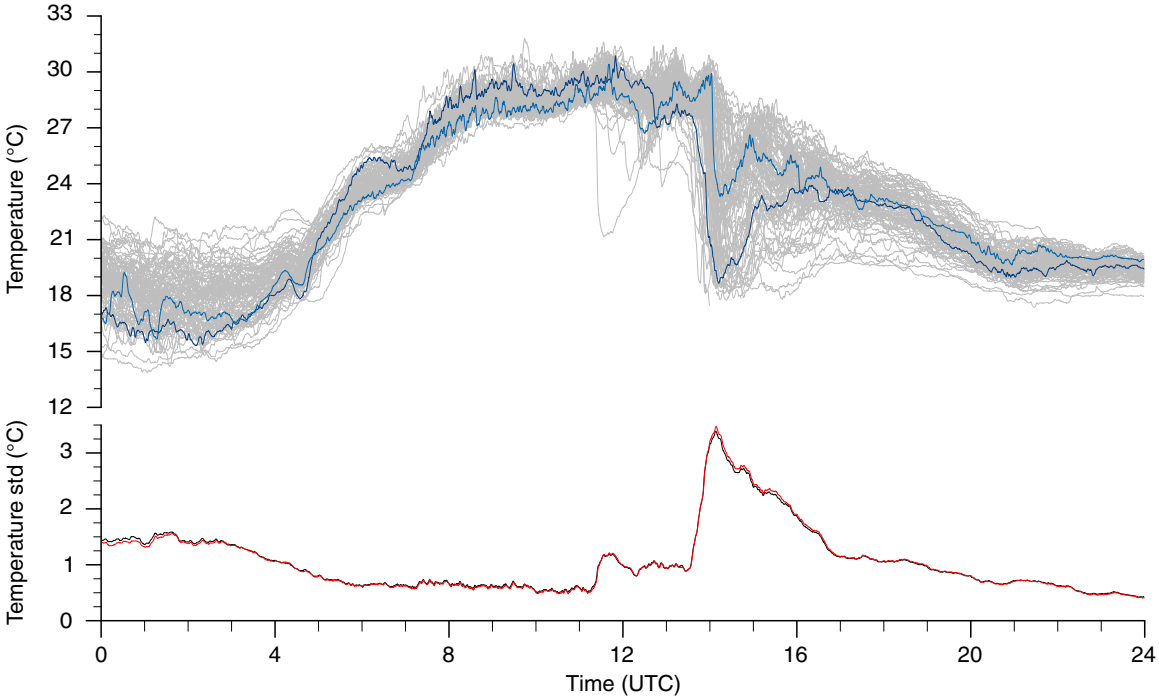

Fig. 3. Time series of (top) temperature and (bottom) its standard deviation across the network measured at the APOLLOs and WXT stations on 29 Jun 2021. Cold pool passage can be recognized by the strong drop in temperature around 1330 UTC [or 1530 Central European summer time (CEST)]. Blue-colored lines highlight the propagation of the cold pool between two stations distanced by 7.2 km. The red line shows the variability computed by removing stations closer than 1 km to each other.

(e.g., Kirsch et al. 2021; Kruse et al. 2022), the temperature perturbation decreases with height. Obvious variability nevertheless exists across supersites. The signal is strongest and longer lasting in Birkholz, followed by Lindenberg and finally GM Falkenberg. This is consistent with their respective location relative to the cold pool core (see Fig. 4).

The FESSTVaL temperature measurements not only revealed the internal variability and morphology of cold pools in three dimensions, but the combination of different measurements raises the question of the definition of a cold pool, a question that could only be answered

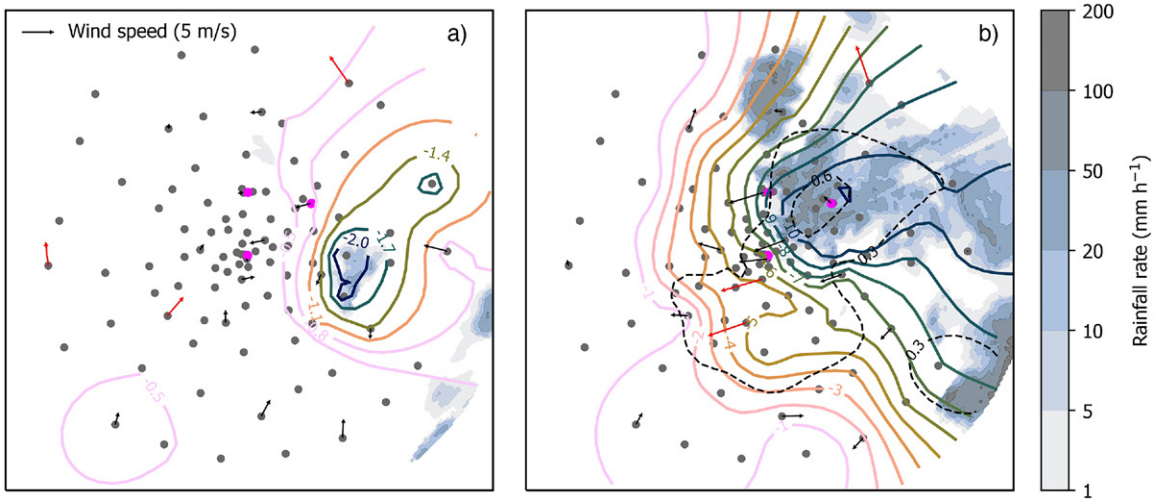

Fig. 4. Two-dimensional horizontal view of a cold pool captured at (a) 1321 and (b) 1416 UTC 29 Jun 2021. Displayed are temperature (solid colored lines) and pressure (black dashed lines) perturbations measured by the APOLLOs and WXTs, as well as precipitation (shading) from the X-band radar and wind from the WXTs. Red arrows for the three largest wind speeds. Magenta circles indicate the locations of the three supersites. Note the different temperature contour intervals on the two plots.

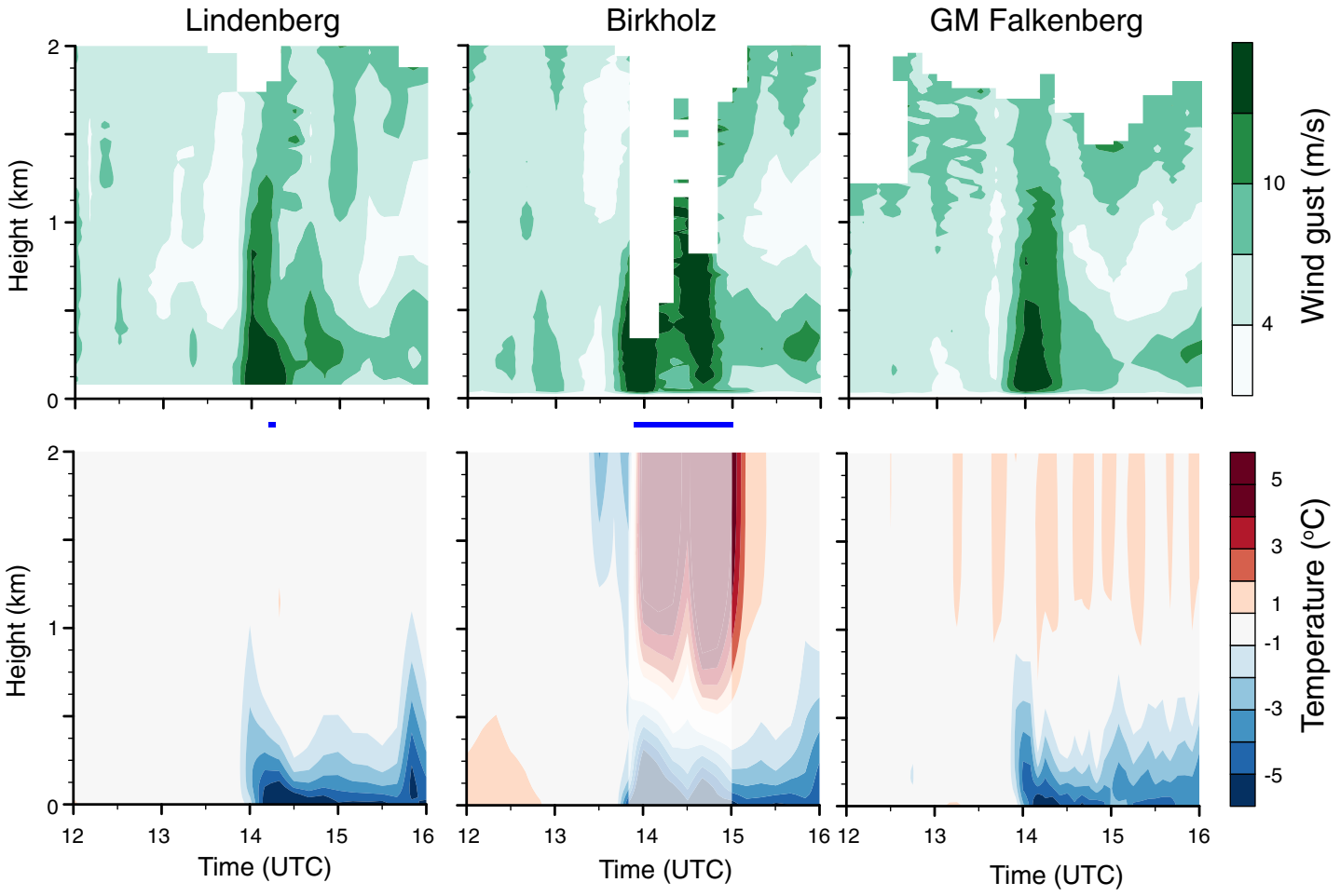

Fig. 5. Time–height plot of (top) wind gust and (bottom) temperature perturbation measured at the three supersites — (left) Lindenberg, (center) Birkholz, and (right) GM Falkenberg—on 29 Jun 2021, together with duration of recorded rain at the corresponding WXT station (blue horizontal bar between the two rows). Wind gusts are retrieved from Doppler lidars employ-ing the algorithm developed by Steinheuer et al. (2022) and temperature profiles, plotted as deviation from the temperature profile recorded at 1300 UTC, are retrieved from the microwave radiometers. Cold pool passage with strong winds and cold temperatures are visible around 1400 UTC. In Birkholz, colors are faded out on the temperature plot between 1350 and 1500 UTC due to the presence of rain drops on the radome.

from model simulations previously (e.g., Drager and van den Heever 2017): What is a cold pool? Where is its edge? And what is its vertical extent? Temperature, pressure, and wind all react to the passage of the cold pool, but the resulting spatial anomalies do not necessarily match (Fig. 4). In the horizontal, the temperature perturbation covers the largest area and is the longest-lasting signal. The strongest pressure perturbation tends to be correlated with the strongest temperature perturbation (Fig. 4b) but is not always apparent (Fig. 4a). Likewise, strong winds are present in the vicinity of the cold pool, but the strongest winds, as visualized by the red arrows in Fig. 4, are not situated close to the edge of the cold core of the cold pool. Another way to define the edge of a cold pool is by the location of newly triggered convective cells. This tends to happen at the edge of existing cold pools (e.g., Schlemmer and Hohenegger 2014; Hirt et al. 2020), even though some ambiguity remains as other processes (gravity waves, local convergence lines) can as well trigger new cells. The X-band radar also captured the triggering of a new cell, but it is located at the edge of the 6-K temperature perturbation isoline in Fig. 4b. Likewise, the difficulty in objectively defining the extent of a cold pool also concerns its depth (Fig. 5). Wind gusts stronger than 7 m s^{-1}, the typical wind speed before the arrival of the cold pool, extend well above 1 km, even above 1.5 km in Lindenberg and GM Falkenberg when looking at the vertical extent of the sharp temporal wind gust gradient.

This is deeper than the retrieved temperature perturbation. Hence, from the deployed instruments, we conclude that determining the precise location of the edge of a cold pool may require a high-density network given the observed sharp gradients, but this location may anyway end up being rather subjective and specific to the process/variable considered.

Validating submesoscale variability

DWD conducts its operational limited-area weather forecasts with the ICOsahedral Nonhydrostatic (ICON) model (Zängl et al. 2015). Operational forecasts are available at a grid spacing of 2.2 km (ICON-DE) over a domain covering Germany, Switzerland, Austria, and part of the neighboring countries, as well as at a grid spacing of 6.5 km (ICON-EU) over Europe for the duration of FESSTVaL. Additional simulations were conducted for a subset of days to further study the sensitivity of simulated submesoscale variability to grid spacing and model parameterization choices. First, a suite of simulations with the same model configuration as ICON-DE were conducted at a grid spacing of 1.2, 2.5, and 5 km. The integration domain is circular, centered at GM Falkenberg, with a radius of about 274 km, and the lateral boundary conditions are provided by ICON-EU. Second, simulations using the large-eddy configuration of ICON (Dipankar et al. 2015) were conducted with a grid spacing of 75, 125, 300, and 600 m. Their integration domain only covers a radius of about 12 km around GM Falkenberg, whereas the lateral boundary conditions are provided by ICON-DE. The large-eddy configuration employs a different turbulence scheme and does not employ parameterizations for shallow convection, subgrid-scale orographic drag, and gravity wave drag. The validation against observations of, for instance, the morphology of cold pools is challenging due to the chaotic nature of convection and the limited number of cases available. To bypass this, a focus will be on validating relationships, for instance, between precipitation and cold pool strength. Moreover, the wealth of observations and some of the new retrievals, especially providing vertical profiles of wind gusts and turbu-lent kinetic energy, will be used for testing new parameterization developments, also in a single-column modeling framework.

Concluding thoughts

FESSTVaL demonstrated the usefulness of dense surface observational networks of low-cost and self-developed instruments to augment the measurement density, allowing to better resolve and study submesoscale atmospheric phenomena like cold pools. If one thing should be changed, then a larger measurement area would be beneficial as in only one event, the cold pool stayed within the circle during its whole life cycle. Enlarging the measurement area would require reducing the maintenance requirement of the APOLLOs due to the needed frequent recharging of their batteries. This could be achieved either by reducing the sampling frequency from 1 to 10 s, which seems fully adequate, by using solar panels, with may increase vandalism, or by involving citizens. In terms of network design, the distribution of stations, being more regular, like in FESSTVaL, or irregular, like in Kirsch et al. (2022b), seems irrelevant. The optimal spacing between stations requires further analysis and might end up as a compromise between measurement area and mea-surement density. At least for the presented cold pool event, removing eight APOLLOs from the more densely packed region of the FESSTVaL circle had only a minimal impact on the computed temperature variability (see red line in Fig. 3). Having more than one supersite to sample the vertical structure of the atmosphere is necessary, and having three seems a bare minimum. One question that will be difficult to answer from the FESSTVaL data is how the depth of the cold pool varies as it propagates. Deploying the fleet of drones over a larger area than the GM Falkenberg field could enhance the vertical network. However, given the requested human supervision and the infrequent convective development over

Germany, such a strategy may work better in an environment like the U.S. Great Plains, as in C^3LOUD-Ex, whereas relying on citizens may work better in a more densely populated place like Germany.

We hope that the high spatial and temporal resolution of our data will be of interest for other applications, and that the developed low-cost instruments will be deployed in future field campaigns to obtain better statistics of cold pool properties. Such data could help to validate and develop postprocessing algorithms for the already existing and dense Netatmo network of personal weather stations, or to train retrievals of cold pools by satellites. At least in Europe, given the infrequent and localized nature of convection, the most important as-pect when designing future field campaigns is to sample the atmosphere for a full summer season. Perhaps as a second-most-important aspect, experimenting with an inexpensive way of measuring 2-m specific humidity would be of interest given the debated existence of moist rings around cold pools, and would also further contribute to the discussion of what a cold pool is and where it does end.

Acknowledgments. FESSTVaL was initiated and supported by the Hans Ertel Centre for Weather Research, a research network of universities, research institutes, and the Deutscher Wetterdienst funded by the Federal Ministry of Transport and Digital Infrastructure (BMVI). We acknowledge the Integrated Climate Data Center (ICDC) for storage of the FESSTVaL data as well as DKRZ for use of its computer resources to perform and store the simulations. We thank the three reviewers for their thorough review and helpful comments.

Data availability statement. All the data are freely available and can be downloaded from https://www.cen.uni-hamburg.de/en/icdc/data/atmosphere/samd-st-datasets/samd-st-fesstval.html.

Appendix A: Specification of measurements and instruments

This appendix contains Tables A1–A5, which summarize specific characteristics of the involved instruments and observations taken during FESSTVaL.

Appendix B: Citizen science in atmospheric sciences

Citizen science is the involvement of the public in scientific research [Citizen Science Associ-ation (CSA), http://www.citizenscience.org]. It has a long tradition, e.g., the “Christmas Bird Counting” started in December 1900 in the United States. Also, meteorologists profit from laypeople’s weather observations, be it eye observations from volunteers or crowdsourcing from citizens’ automated weather station deployed in their garden. The degree of participa-tion can greatly vary from collecting automatically recorded instrument data from citizens’ devices (crowdsourcing) to involving laypeople in the design of the research project. The Hans Ertel Centre for Weather Research uses citizen science approaches not only to collect atmospheric data but also to develop warning formats for extreme weather events.

Table A1. Summary of surface measurements specifically conducted during FESSTVaL. Specifications taken from the corresponding sensor manuals. The commercial instruments WXTs and the soil sensors were provided by Vaisala and by Scanntronik (Germany), respectively. Soil moisture is derived by measuring the dielectric permittivity ϵ. Abbreviations are as follows: SW, shortwave; LW, longwave; EB, energy balance; RH, relative humidity; θ_z, zenith angle; NA, not available. The "project" column indicates which type of submesoscale variability was targeted by each instrument: CP, cold pool; WG, wind gust; RAD, radiation; SM, soil moisture; CS, citizen science.

Instrument	Parameter	Sensor	Location	Measurement range	Accuracy	Sampling	Project
WXT	Temperature	PTU module	Circle	–52° to 60°C	±0.3 K at 20°C	10 s	CP
WXT	Pressure	PTU module	Circle	500 to 1,100 hPa	±0.5 hPa at 0° to –30°C ±1.0 hPa at –52° to 60°C	10 s	CP
WXT	Relative humidity	PTU module	Circle	0% to 100%	±3% RH at 0% to 90% ±5% RH at 90% to 100%	10 s	CP
WXT	Wind speed	Ultrasonic anemo.	Circle	0 to 60 m s^{-1}	±3% at 10 m s^{-1}	10 s	CP, WG
WXT	Wind direction	Ultrasonic anemo.	Circle	0° to 360°	±3° at 10 m s^{-1}	10 s	CP, WG
WXT	Rainfall	Piezoelectrical sensor	Circle	—	Better than 5%	10 s	CP
APOLLO	Temperature	NTC thermistor	Circle	–40° to 100°C	±0.2 K at 0° to 70°C	1 s	CP
APOLLO	Pressure	BME280	Circle	300 to 1,100 hPa	±1.0 hPa at 0° to 30°C ±0.12 hPa at 25° to 40°C	1 s	CP
MESSI	Temperature	PT1000	Circle	–50° to 300°C	±0.2 K at 0° to 70°C	10 s	CP, CS
MESSI	Pressure	BMP38x	Circle	300 to 1,100 hPa	0.5 hPa at 0° to 65°C	10 s	CP, CS
MESSI	Relative humidity	SHT31	Circle	0% to 100%	±2%	10 s	CP, CS
Soil sensor	Skin temperature	Soil Analysis Sensor	Circle	–30° to 120°C	±1°C	5 min	CP
			GM Falkenberg			10 min	CP, SM
Soil sensor	Soil temperature	Soil Analysis Sensor	Circle	–30° to 80°C	±1°C	5 min	CP
			GM Falkenberg			10 min	CP, SM
Soil sensor	Soil moisture	Soil Analysis Sensor	Circle	ϵ = 1 to 80	ϵ = ±1 at 1 to 40 ±15% at ϵ = 40 to 80	5 min	CP
			GM Falkenberg			10 min	CP, SM
FROST	Solar Radiation	AMS AS7265x	GM Falkenberg	410 to 940 nm	2.5% for θ_z < 75°	10 Hz	RAD
EB station	Temperature	HMT337	Birkholz	–70° to 180°C	±0.2 K at 20°C	1 min	CP
EB station	Pressure	PTB200A	Birkholz	600 to 1,100 hPa	±0.12 hPa	1 min	CP
EB station	Relative humidity	HMT337	Birkholz	0% to 100%	±1% to 2% at 20°C	1 min	CP
EB station	Water vapor	LI-7500	Birkholz	0 to 42 g m^{-3}	NA	0.05 s	CP
EB station	Wind (3D)	USA-1 Scientific	Birkholz	–50 to 50 m s^{-1}	NA	0.05 s	CP
EB station	SW radiation	CNR4	Birkholz	0 to 2,000 W m^{-2}	<15 W m^{-2}	1 min	CP, RAD
EB station	LW radiation	CNR4	Birkholz	–250 to 250 W m^{-2}	<10 W m^{-2}	1 min	CP, RAD
EB station	Soil heat flux	HFP01	Birkholz	–2,000 to 2,000 W m^{-2}	±3%	1 min	CP

Table A2. Summary of measurements from vertical/horizontal profiling instruments specifically installed for FESSTVaL. Abbreviations are as follows: IWV, vertically integrated water vapor; LWP, liquid water path; TKE, turbulent kinetic energy; *T*, temperature; RH, relative humidity; qv, specific humidity; *p*, pressure; *u*, zonal wind component; *υ*, meridional wind component; *w*, vertical wind; CSM, continuous scanning mode; RHI, range height indicator; PPI, plan position indicator; VAD24, velocity azimuth display with 24 scanning beams. No entry in the "time period" column means the variable was measured during the full duration of FESSTVaL. The "project" column indicates which type of submesoscale variability was targeted by each instrument: CP, cold pool; WG, wind gust; CPA, coherent pattern; LLJ, low-level jet.

Instrument	Parameter	Scan mode	Location	Time period	Project
RPG HATPRO	*T*	Elevation scan	Triangle		CP, LLJ
RPG HATPRO	Water vapor	Vertical stare	Triangle		CP
RPG HATPRO	IWV, LWP	Vertical stare	Triangle		CP
RPG HATPRO	IWV, LWP	Azimuth scan	Lindenberg		CP
HALO Streamline	Wind gust, mean wind	Fast CSM, 3.4 s	Triangle	11 Jun–14 Jul, 10 –31 Aug	CP, WG, LLJ
HALO Streamline	TKE, mean wind	Slow CSM, 72 s	GM Falkenberg	18 May–15 Jul, 2–27 Aug	CP, CPA
Leosphere WindCube	Wind	RHI/PPI	GM Falkenberg	17 May–27 Aug	CPA
HALO Streamline	*w*	Vertical stare	GM Falkenberg	18 May–15 Jul, 10–27 Aug	CP
HALO Streamline	Mean wind	VAD24, 2 min	GM Falkenberg	2 Jun–15 Jul	LLJ
HALO Streamline	Mean wind	VAD24, 2 min	Lindenberg	17 May–15 Jul	LLJ
ASSIST	*T*	Vertical stare	Lindenberg		CP, LLJ
ASSIST	Water vapor	Vertical stare	Lindenberg		CP
ASSIST	LWP	Vertical stare	Lindenberg		CP
ATMONSYS	*T*, qv, aerosol	Vertical stare	Lindenberg	19 Jun–21 Jul	CPA
X-band radar	Rainfall rate	20-km scan radius	GM Falkenberg	3 Jun–30 Aug	CP
SWUF-3D	*p*, *T*, *u*, *υ*, *w*, qv		GM Falkenberg	21 Jun–2 Jul	CPA
MASC-3	*p*, *T*, *u*, *υ*, *w*, qv, TKE		GM Falkenberg	7 Jun–2 Jul	CPA
Radiosonde	*p*, *T*, wind, RH		Lindenberg, GM Falkenberg		CP, WG, LLJ

Table A3. Additional radiosondes launched during FESSTVaL. Operational radiosondes are launched by DWD from Lindenberg every day at 0445, 1045, 1645, and 2245 UTC. UAS stands for uncrewed aerial system.

Date	Time (UTC)	Comment
27 May	1540	Test
8 Jun	1615	Test
10 Jun	0645, 0845, 1245, 1445	UAS flight
14 Jun	0630, 1330	UAS flight
17 Jun	0745	UAS flight
19 Jun	1330	Cold pool
29 Jun	0645, 0845, 1245, 1400, 1600	Cold pool
1 Jul	0800	For movie making
5 Jul	1521	Cold pool
9 Jul	1322, 1704	Cold pool
13 Jul	2046	Cold pool
17 Jul	1230	Cold pool
25 Jul	1438, 1605	Cold pool
10 Aug	1230, 1830	Cold pool
11 Aug	1950	Surface inversion of nocturnal boundary layer
12 Aug	0250, 1950	Surface inversion of nocturnal boundary layer
13 Aug	0250	Surface inversion of nocturnal boundary layer
17 Aug	1323	Wind gust

Table A4. List of SWUF-3D flights with flight patterns. The flight patterns are vert: vertical profile with six stationary drones on top of each other; hor: horizontal profile with several stationary drones (usually 10) at one height; vprof: vertical profile with one vertically moving drone; cal: calibration flight with 10 drones close to the DWD meteorological tower at the altitudes of the sonic anemometer measurements; vad: validation flight with several drones along the scanning cone of lidars. These flight patterns were associated with different mission types: stratification, targeting the thermal stratification of the boundary layer and turbulence profiles; morning transition (from night into day); coherence, with the aim to analyze spatial correlation and coherence; cold pool; lidar validation as a proof-of-concept to show that drones are a very good tool to compare lidars retrieval accuracy; calibration to calibrate the drones with the help of the sonic anemometer measurements from the meteorological tower.

Date	Time (UTC)	Flight pattern	Mission type
21 Jun	1516	vert	Stratification
22 Jun	1000, 1030, 1235, 1254	vert	Stratification
22 Jun	1400, 1540	hor	Coherence
23 Jun	0750, 0835, 1411, 1434, 1504, 1543	cal	Calibration
23 Jun	0957, 1020, 1054, 1204, 1230	hor	Coherence
25 Jun	0713, 0908, 0934	cal	Calibration
25 Jun	0742, 0812, 0958, 1200, 1240, 1335	hor+vprof	Coherence
25 Jun	1214, 1255, 1356, 1553, 1556	hor	Coherence
26 Jun	0657, 0720, 0921, 0950	cal	Calibration
26 Jun	0832, 1039, 1042	hor	Coherence
27 Jun	1300, 1310, 1320	vert+vprof	Stratification
27 Jun	1409	vad	Lidar validation
27 Jun	1454, 1507, 1556	hor	Coherence
27 Jun	1544	hor+vprof	Stratification
28 Jun	0354, 0404, 0414, 0425, 0435, 0447, 0457, 0509, 0520, 0532, 0543, 0554, 0606, 0618, 0630, 0641, 0654, 0705, 0717, 0729, 0740, 0752, 0804	vert+vprof	Morning transition
29 Jun	0354, 0407, 0457, 0510, 0552, 0618, 1351, 1402	hor	Morning transition
29 Jun	0356, 0413, 0438, 0505, 0516, 0548, 0559, 0621, 1354	vprof	Morning transition
29 Jun	0420, 0443, 0604	hor+vprof	Morning transition
29 Jun	0730	cal	Calibration
29 Jun	1237, 1239, 1306, 1307	vad	Lidar validation
29 Jun	1351, 1405	hor+vprof	Cold pool
30 Jun	1457, 1528, 1734, 1758	cal	Calibration
30 Jun	1605, 1652, 1705	hor+vprof	Coherence
30 Jun	1619	hor	Coherence
1 Jul	0654, 1637, 1705	cal	Calibration
1 Jul	0719, 1538	vad	Lidar validation
2 Jul	0708, 0907, 1106, 1322, 1352	cal	Calibration
2 Jul	0802, 1150, 1229, 1512	hor	Coherence
2 Jul	0842, 1422, 1448	vad	Lidar validation
2 Jul	1136, 1217	hor+vprof	Coherence

Table A5. Days with MASC-3 flight measurements and corresponding flight patterns. The flight patterns are lid: lidar validation flight with either 30-min flight sections at two selected altitudes or 10-min flight sections at five to six altitudes covering a distance of 2.5–3 km; BL: boundary layer flight with an ascent up to the top of the planetary boundary layer and then a 15-min descent with level flight legs at four to six predefined altitudes.

Date	Time (UTC)	Flight
7 Jun	1123–1416	lid
8 Jun	0726–0856, 1030–1154	lid
9 Jun	0839–0951	lid
9 Jun	1153–1305	BL
10 Jun	0714–0832, 0924–1033, 1213–1330, 1356–1445	BL
11 Jun	0829–1001, 1107–1205, 1751–1916	lid
13 Jun	1130–1240, 1327–1440	lid
13 Jun	1704–1759	BL
14 Jun	0505–0605, 0703–0818, 1157–1258, 1457–1546	BL
15 Jun	0923–1036, 1533–1639	lid
16 Jun	0841–0944, 1213–1315, 1800–1930	lid
17 Jun	0753–0920, 1211–1302, 1452–1635	BL
18 Jun	1036–1142	lid
19 Jun	0621–0736, 0823–0905	lid
21 Jun	1248–1416	lid
23 Jun	0825–0955, 1533–1652	lid
24 Jun	0855–1010	lid
25 Jun	0833–0924, 1016–1156, 1417–1541	lid
26 Jun	0631–0804, 0908–1035	lid
28 Jun	1451–1545	lid
29 Jun	0747–0920	BL
29 Jun	1005–1120	lid
1 Jul	1759–1924	lid
2 Jul	0930–1105, 1258–1418, 1653–1800	lid

References

Beyrich, F., H.-J. Herzog, and J. Neisser, 2002: The LITFASS project of DWD and the LITFASS-98 experiment: The project strategy and the experimental setup. *Theor. Appl. Climatol.*, **73**, 3–18, https://doi.org/10.1007/s00704-002-0690-8. Böing, S. J., H. J. J. Jonker, A. P. Siebesma, and W. W. Grabowski, 2012: Influence of the subcloud layer on the development of a deep convective ensemble. *J. Atmos. Sci.*, **69**, 2682–2698, https://doi.org/10.1175/JAS-D-11-0317.1. Brock, F. V., K. C. Crawford, R. L. Elliott, G. W. Cuperus, S. J. Stadler, H. L. Johnson,

and M. D. Eilts, 1995: The Oklahoma Mesonet: A technical overview. *J. Atmos. Oceanic Technol.*, **12**, 5–19, https://doi.org/10.1175/1520-0426(1995)012<0005:TOMATO>2.0.CO;2.

Burgemeister, F., M. Clemens, and F. Ament, 2022: Rainfall rates estimated from X-Band radar observations during FESSTVaL 2021. Universität Hamburg, accessed 1 April 2023, https://doi.org/10.25592/uhhfdm.10090.

Clark, M. R., J. D. C. Webb, and P. J. Kirk, 2018: Fine-scale analysis of a severe hailstorm using crowd-sourced and conventional observations. *Meteor. Appl.*, **25**, 472–492, https://doi.org/10.1002/met.1715.

Corfidi, S. F., 2003: Cold pools and MCS propagation: Forecasting the motion of downwind-developing MCSs. *Wea. Forecasting*, **18**, 997–1017, https://doi.org/10.1175/1520-0434(2003)018<0997:CPAMPF>2.0.CO;2.

Crewell, S., and U. Löhnert, 2007: Accuracy of boundary layer temperature profiles retrieved with multi-frequency, multi-angle microwave radiometry. *IEEE Trans. Geosci. Remote Sens.*, **45**, 2195–2201, https://doi.org/10.1109/TGRS.2006.888434.

Detring, C., E. Päschke, M. Kayser, R. Leinweber, and F. Beyrich, 2022: Deriving wind gust from Doppler lidar measurements. *EMS Annual Meeting Abstracts*, Vol. 19, EMS2022-184, https://doi.org/10.5194/ems2022-184.

——, F. Beyrich, J. Steinheuer, M. Kayser, R. Leinweber, U. Löhnert, and E. Päschke, 2023: Ultrasonic anemometer and Doppler lidar wind and gust data products during FESSTVAL 2021. Universität Hamburg, accessed 1 April 2023, https://doi.org/10.25592/uhhfdm.11227.

Dewani, N., and R. Leinweber, 2022: Vertical velocity data from vertical stare Doppler lidar, Falkenberg, FESSTVaL campaign 2020/2021. Universität Hamburg, accessed 1 April 2023, https://doi.org/10.25592/uhhfdm.10385.

Dipankar, A., B. Stevens, R. Heinze, C. Moseley, G. Zängl, M. Giorgetta, and S. Brdar, 2015: Large eddy simulation using the general circulation model ICON. *J. Adv. Model. Earth Syst.*, **7**, 963–986, https://doi.org/10.1002/2015MS000431.

Drager, A. J., and S. C. van den Heever, 2017: Characterizing convective cold pools. *J. Adv. Model. Earth Syst.*, **9**, 1091–1115, https://doi.org/10.1002/2016MS000788.

Grabowski, W. W., and Coauthors, 2006: Daytime convective development over land: A model intercomparison based on LBA observations. *Quart. J. Roy. Meteor. Soc.*, **132**, 317–344, https://doi.org/10.1256/qj.04.147.

Grell, G. A., L. Schade, R. Knoche, A. Pfeiffer, and J. Egger, 2000: Nonhydrostatic climate simulations of precipitation over complex terrain. *J. Geophys. Res.*, **105**, 29 595–29 608, https://doi.org/10.1029/2000JD900445.

Haerter, J. O., S. J. Böing, O. Henneberg, and S. B. Nissen, 2019: Circling in on convective organization. *Geophys. Res. Lett.*, **46**, 7024–7034, https://doi.org/10.1029/2019GL082092.

Heusinkveld, B. G., B. M. Wouter, and C. C. van Heerwaarden, 2022: A new accurate low-cost instrument for fast synchronized spatial measurements of light spectra. *Atmos. Meas. Tech.*, **16**, 3767–3785, https://doi.org/10.5194/amt-16-3767-2023.

Hirt, M., G. C. Craig, S. A. K. Schäfer, J. Savre, and R. Heinze, 2020: Cold-pool-driven convective initiation: Using causal graph analysis to determine what convection-permitting models are missing. *Quart. J. Roy. Meteor. Soc.*, **146**, 2205–2227, https://doi.org/10.1002/qj.3788.

Houston, A. L., B. Argrow, J. Elston, J. Lahowetz, E. W. Frew, and P. C. Kennedy, 2012: The Collaborative Colorado–Nebraska Unmanned Aircraft System Experiment. *Bull. Amer. Meteor. Soc.*, **93**, 39–54, https://doi.org/10.1175/2011BAMS3073.1.

Houze, R. A. J., 2004: Mesoscale convective systems. *Rev. Geophys.*, **42**, 6885–6904, https://doi.org/10.1029/2004RG000150.

Jung, S., J. Boventer, A. Platis, and J. Bange, 2023: Fixed-wing UAS wind and turbulence measurements at GM Falkenberg during FESSTVaL 2020 and 2021. Universität Hamburg, accessed 1 April 2023, https://doi.org/10.25592/uhhfdm.11229.

Khairoutdinov, M., and D. Randall, 2006: High-resolution simulation of shallow-to-deep convection transition over land. *J. Atmos. Sci.*, **63**, 3421–3436, https://doi.org/10.1175/JAS3810.1.

Kirsch, B., F. Ament, and C. Hohenegger, 2021: Convective cold pools in long-term boundary layer mast observations. *Mon. Wea. Rev.*, **149**, 811–820, https://doi.org/10.1175/MWR-D-20-0197.1.

——, C. Hohenegger, D. Klocke, and F. Ament, 2022a: Meteorological network observations by APOLLO and WXT weather stations during FESSTVaL 2021. Universität Hamburg, accessed 1 April 2023, https://doi.org/10.25592/uhhfdm.10179.

——, ——, ——, R. Senke, M. Offermann, and F. Ament, 2022b: Sub-mesoscale observations of convective cold pools with a dense station network in Ham-burg Germany. *Earth Syst. Sci. Data*, **14**, 3531–3548, https://doi.org/10.5194/essd-14-3531-2022.

——, B. Stiehle, U. Löhnert, and F. Ament, 2022c: Radiosonde profile measurements during FESSTVaL 2021. Universität Hamburg, accessed 1 April 2023, https://doi.org/10.25592/uhhfdm.10279.

Kox, T., H. W. Rust, B. Wentzel, M. Göber, C. Böttcher, J. Lehmke, and M. Garschagen, 2021: Build and measure: Students report weather impacts and collect weather data using self-built weather stations. *Australas. J. Disaster Trauma Stud.*, **25**, 79–86, https://trauma.massey.ac.nz/issues/2021-3/AJDTS_25_3_Kox.pdf.

Kruse, I. L., J. O. Haerter, and B. Meyer, 2022: Cold pools over the Netherlands: A statistical study from tower and radar observations. *Quart. J. Roy. Meteor. Soc.*, **148**, 711–726, https://doi.org/10.1002/qj.4223.

Lange, I., and F. Ament, 2022: Standard meteorology pressure, temperature, humidity, radiation fluxes and soil heat flux, and turbulent fluxes (2021) from FESSTVaL Supersite in Birkholz, Germany. Universität Hamburg, accessed 1 April 2023, https://doi.org/10.25592/uhhfdm.10563.

Leinweber, R., F. Meier, and F. Beyrich, 2023: Doppler lidar mean wind profiles from VAD scans during FESSTVAL 2021. Universität Hamburg, accessed 1 April 2023, https://doi.org/10.25592/uhhfdm.11394.

Lengfeld, K., M. Clemens, H. Münster, and F. Ament, 2014: Performance of high-resolution X-band weather radar networks–The pattern example. *Atmos. Meas. Tech.*, **7**, 4151–4166, https://doi.org/10.5194/amt-7-4151-2014.

Löhnert, U., C. Knist, T. Böck, and B. Pospichal, 2022: Microwave radiometer observations during FESSTVaL 2021. Universität Hamburg, accessed 1 April 2023, https://doi.org/10.25592/uhhfdm.10198.

Mandement, M., and O. Caumont, 2020: Contribution of personal weather stations to the observation of deep-convection features near the ground. *Nat. Hazards Earth Syst. Sci.*, **20**, 299–322, https://doi.org/10.5194/nhess-20-299-2020.

Mass, C. F., D. Ovens, K. Westrick, and B. A. Colle, 2002: Does increasing horizontal resolution produce more skillful forecasts? *Bull. Amer. Meteor. Soc.*, **83**, 407–430, https://doi.org/10.1175/1520-0477(2002)083<0407:DIHRPM>2.3.CO;2.

Mc Pherson, R. A., and Coauthors, 2007: Statewide monitoring of the mesoscale environment: A technical update on the Oklahoma Mesonet. *J. Atmos. Oceanic Technol.*, **24**, 301–321, https://doi.org/10.1175/JTECH1976.1.

Mol, W., and B. Heusinkveld, 2022: Radiometer grid at Falkenberg and surroundings, downwelling shortwave radiation, FESSTVaL campaign. Universität Hamburg, accessed 1 April 2023, https://doi.org/10.25592/uhhfdm.10273.

Morrison, J., J. M. Peters, K. K. Chandrakar, and S. C. Sherwood, 2022: Influences of environmental relative humidity and horizontal scale of subcloud ascent on deep convective initiation. *J. Atmos. Sci.*, **79**, 337–359, https://doi.org/10. 1175/JAS-D-21-0056.1.

Päschke, E., 2022: FESSTVaL Falkenberg Doppler lidar 30 minutes mean wind and turbulence profiles. Universität Hamburg, accessed 1 April 2023, https://doi.org/10.25592/uhhfdm.10559.

Rautenberg, A., and Coauthors, 2019: The multi-purpose airborne sensor carrier MASC-3 for wind and turbulence measurements in the atmospheric boundary layer. *Sensors*, **19**, 2292, https://doi.org/10.3390/s19102292.

Rochetin, N., C. Hohenegger, L. Touzé-Peiffer, and N. Villefranque, 2021: A physically-based definition of convectively generated density currents: Detection and characterization in convection-permitting simulations. *J. Adv. Model. Earth Syst*., **13**, e2020MS002402, https://doi.org/10.1029/2020MS002402.

Romps, D. M., and N. Jeevanjee, 2019: On the sizes and lifetimes of cold pools. *Quart. J. Roy. Meteor. Soc.*, **142**, 1517–1527, https://doi.org/10.1002/qj.2754.

Schlemmer, L., and C. Hohenegger, 2014: The formation of wider and deeper clouds as a result of cold-pool dynamics. *J. Atmos. Sci.*, **71**, 2842–2858, https://doi.org/10.1175/JAS-D-13-0170.1.

Smalikho, I. N., and V. A. Banakh, 2017: Measurements of wind turbulence parameters by a conically scanning coherent Doppler lidar in the atmospheric boundary layer. *Atmos. Meas. Tech.*, **10**, 4191–4208, https://doi.org/10.5194/amt-10-4191-2017.

Soderholm, J., H. McGowan, H. Richter, K. Walsh, T. Weckwerth, and M. Coleman, 2016: The Coastal Convective Interactions Experiment (CCIE): Understanding the role of sea breezes for hailstorm hotspots in eastern Australia. *Bull. Amer. Meteor. Soc.*, **97**, 1687–1698, https://doi.org/10.1175/BAMS-D-14-00212.1.

Steinheuer, J., C. Detring, F. Beyrich, U. Löhnert, P. Friederichs, and S. Fiedler, 2022: A new scanning scheme and flexible retrieval for mean winds and gusts from Doppler lidar measurements. *Atmos. Meas. Tech.*, **15**, 3243–3260, https://doi.org/10.5194/amt-15-3243-2022.

Stevens, B., and Coauthors, 2019: DYAMOND: The DYnamics of the Atmospheric general circulation Modeled on Non-hydrostatic Domains. *Prog. Earth Planet. Sci.*, **6**, 61, https://doi.org/10.1186/s40645-019-0304-z.

Straka, J. M., E. N. Rasmussen, and S. E. Fredrickson, 1996: A mobile mesonet for finescale meteorological observations. *J. Atmos. Oceanic Technol.*, **13**, 921–936, https://doi.org/10.1175/1520-0426(1996)013<0921:AMMFFM>2.0.CO;2.

Suomi, I., S.-E. Gryning, E. J. O'Connor, and T. Vihma, 2017: Methodology for obtaining wind gusts using Doppler lidar. *Quart. J. Roy. Meteor. Soc.*, **143**, 2061–2072, https://doi.org/10.1002/qj.3059.

Turner, D., and L. Rochette, 2022: Thermodynamic retrieved profiles from the ASSIST infrared spectrometer, FESSTVaL campaign. Universität Hamburg, accessed 1 April 2023, https://doi.org/10.25592/uhhfdm.10212.

Turner, D. D., and U. Löhnert, 2021: Ground-based temperature and humidity profiling: Combining active and passive remote sensors. *Atmos. Meas. Tech.*, **14**, 3033–3048, https://doi.org/10.5194/amt-14-3033-2021.

van den Heever, S. C., and Coauthors, 2021: The Colorado State University Convective CLoud Outflows and UpDrafts Experiment (C^3LOUD-Ex). *Bull. Amer. Meteor. Soc.*, **102**, E1283–E1305, https://doi.org/10.1175/BAMS-D-19-0013.1.

Wakimoto, R. M., 1982: The life cycle of thunderstorm gust fronts as viewed with Doppler radar and rawinsonde data. *Mon. Wea. Rev.*, **110**, 1060–1082, https://doi.org/10.1175/1520-0493(1982)110<1060:TLCOTG>2.0.CO;2.

Weide Luiz, E., and S. Fiedler, 2022: Spatiotemporal observations of nocturnal low-level jets and impacts on wind power production. *Wind Energy Sci.*, **7**, 1575–1591, https://doi.org/10.5194/wes-7-1575-2022.

Wetz, T., N. Wildmann, and F. Beyrich, 2021: Distributed wind measurements with multiple quadrotor unmanned aerial vehicles in the atmospheric bound-ary layer. *Atmos. Meas. Tech.*, **14**, 3795–3814, https://doi.org/10.5194/amt-14-3795-2021.

——, J. Zink, J. Bange, and N. Wildmann, 2023: Analyses of spatial correlation and coherence in ABL flow with a fleet of UAS. *Bound.-Layer Meteor.*, **187**, 673–701, https://doi.org/10.1007/s10546-023-00791-4.

Wildmann, N., 2022: Multicopter UAS measurements at GM Falkenberg during FESSTVaL 2021. Universität Hamburg, accessed 1 April 2023, https://doi.org/10.25592/uhhfdm.10148.

——, and T. Wetz, 2022: Towards vertical wind and turbulent flux estimation with multicopter uncrewed aircraft systems. *Atmos. Meas. Tech.*, **15**, 5465–5477, https://doi.org/10.5194/amt-15-5465-2022.

Zängl, G., D. Reinert, P. Ripodas, and M. Baldauf, 2015: The ICON (ICOsahedral non-hydrostatic) modelling framework of DWD and MPI-M: Description of the non-hydrostatic dynamical core. *Quart. J. Roy. Meteor. Soc.*, **141**, 563–579, https://doi.org/10.1002/qj.2378.